Journal of Hydraulic Structures
J. Hydraul. Struct., 2023; 9(3): 14-31
DOI: 10.22055/jhs.2023.44699.1262

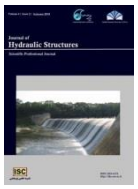

OPEN ACCESS

Simultaneous employment of hydrodynamical simulation and RS imageries for analyzing the influence of an anthropogenic construction on shoreline transformation

Danial Ghaderi [1]
Maryam Rahbani [2]

Abstract

Coastal areas are usually heavily exploited. Numerous anthropogenic constructions are developed along the coastal areas for recreational, economic and/or cultural purposes. They influence the coastal hydrodynamics. Therefore, identifying the source of coastline transformation is essential for controlling these modifications and develop a sustainable coastal area. Simultaneous deployment of numerical modeling and RS imageries is a suitable approach for understanding hydrodynamic processes in coastal areas. In this study, the hydrodynamic condition of the Beris Port area located in the Makran region, north of the Gulf of Oman, has been analyzed using MIKE-21 software package, RS, and GIS techniques. Our results reveal the accretion of 20.97 ha adjacent to the breakwater since 1988. We also found that the shore near the port is heavily accumulated by sediment, while this is not the case for those shore far from the port. According to our results significant wave height is considerably low inside the port, even during the high season of summer, which is due to the construction of the port and the bay shape of the coast. The current speed, inside the port, is also low (0.01 m/s). The current adjacent to the port is in the opposite direction to the main current direction of the region, causing nearshore accretion. Therefore, it is believed that the accretion problem is due to the poor design of the breakwaters' layout. Thus, a new alignment for the breakwater is suggested, taking into account the hydrodynamics and morphodynamics of the area.

Keywords: Beris port, Makran region, MIKE 21, RS technique, Shoreline change.

Received: 02 September 2023; Accepted: 21 October 2023

1. Introduction

Coastal areas have long been a focal point for development and construction. These areas are constantly subjected to hydrodynamic processes, such as wind, waves, and currents, making them highly dynamic [1, 2]. In addition to these natural factors, anthropogenic activities such as the

[1] Faculty of Marine Science and Technology, University of Hormozgan, Bandar Abbas, Iran.
[2] Faculty of Marine Science and Technology, University of Hormozgan, Bandar Abbas, Iran. E-Mail: maryamrahbani@yahoo.com, m_rahbani@hormozgan.ac.ir **(Corresponding author)**

construction of breakwaters, harbors, and groins are responsible for shoreline changes [3, 4]. Thus, for better understanding and sustainably managing these areas, studies are required; especially on the hydrodynamic and sedimentation processes of the area [5]. Numerical modeling serves as a convenient approach for examining and analyzing erosion and deposition processes in coastal areas [6]. Additionally, the utilization of remote sensing (RS) and geographic information system (GIS) techniques proves to be effective for estimating historical shoreline transformation [7, 8].

MIKE 21 software is one of the most common and well-known applications in this field, which has been employed by other researches [9, 10, 11]. The pattern of currents and waves during the winter Shamal wind in the northern part of the Persian Gulf was studied using the Coupled Model Flexible Mesh (FM) [12]. In a study [13] the recent erosion problem around the river delta on the Cox's Bazar coast was investigated using numerical model and RS technique. In the RS section, the authors used Landsat images from 1972-2016 to determine the shoreline position and its transformation. Using numerical modeling (MIKE 21 Shoreline Morphology (SM)), they calculated wave-driven currents and sediment transportation to simulate erosional processes. They claimed the results of the model confirmed the growth of the spit observed in satellite images. Zhang et al. predicted back siltation of a deep-water channel in Lanshan Port area of the Port of Rizhao after dredging. They employed MIKE 21 considering wave, tidal current and sediment modules, and claimed that the results of their study can be a guideline for engineering projects and advancing port dredging operations [14]. There are also studies on shoreline change using RS and GIS techniques including [8-15]. Nassar et al. conducted a study on shoreline change along the North Sinai coast in Egypt [16]. Their results revealed that the use of medium-resolution satellite images and geospatial techniques can provide valuable information about coastal morphodynamics and coastal zone management.

Beris fishing port, on the north coast of the Gulf of Oman (Fig. 1), which deals with serious sediment accumulation influenced by breakwater construction, is the subject of this research. Hajivalie and Soltanpour, studied sedimentation and accretion around the breakwaters of this port and claimed that diffraction point was changed due to the shoreline advancement behind the secondary breakwater (labeled 3 in Fig. 1 E) [17]. They emphasized the accumulation of huge portion of sediment before the entrance. However, further observations showed that the bathymetry around the entrance was also considerably influenced by sedimentation (labeled 2 in Fig. 1 D & E). In other research shoreline changes of this port was calculated, using waves and sediment transport modeling [18]. The results confirmed shoreline advancement just back of the secondary breakwater (labeled 3 in Fig. 1 E). In a numerical modelling research, the pattern of wave and current around Beris Port was studied considering two scenarios of before and after construction of the breakwater over the short period of one month, employing MIKE 21 [6]. According to the authors their results criticized the layout of the breakwater, because it was the reason for developing a turbulence inside the basin. Ghaderi and Rahbani studied the shoreline changes in the Beris Port using RS techniques [19]. They examined shoreline transformation over 30 years and showed that the accumulation of sediment in the northern part of the Beris Port (number 4 in Fig. 1-E) is about 7.44 m/year.

As explained above, sediment accumulation around the northern part and the entrance of the Beris Port is an issue, thus was the subject of several studies so far [18, 19, 6]. In the view of previous studies, we decided to employ a quite new technique of simultaneous employment of numerical model and RS techniques to cover the need for field data. Simulated annual wave and current patterns around the Beris Port from the numerical model, and annual shoreline change from RS techniques are analyzed simultaneously to investigate the erosion/accretion pattern in this port.

2. Methods

2.1. Study area

The area under investigation is located southeast of Iran in Makran [20], along the northern coast of the Gulf of Oman. The main focus of this study is the Beris fishery port at 25.147° N latitude and 61.176° E longitude (Fig. 1 A&B). The fishing port is located 85 km east of the coastal city of Chabahar [18]. This region is adjacent to the Gulf of Oman and is under the influence of the Indian Ocean and the Arabian Sea climate [21, 22]. The tide is mesotidal and semidiurnal with a range of approximately 1.66 m (Fig. 2 A). The wind rose of the region (Fig. 2 B) shows that the south and southwest wind is dominated, with an average speed of 4.6 m/s and maximum speed of 11.8 m/s (Fig. 2 B). According to studies carried out in the Beris Port, the main reason for sediment transport in the area is claimed to be regional currents [18], [19, 6]. Beris Port is composed of two breakwaters, the main breakwater (labeled 1 in Fig. 1 E) is an extension of the coastline in a south-north direction, and the subsidiary breakwater is constructed along east-west direction (labeled 3 in Fig. 1 E). According to the literature [6, 19], the head of the main breakwater and the back of the secondary breakwater are the two areas that severely suffer from sedimentation.

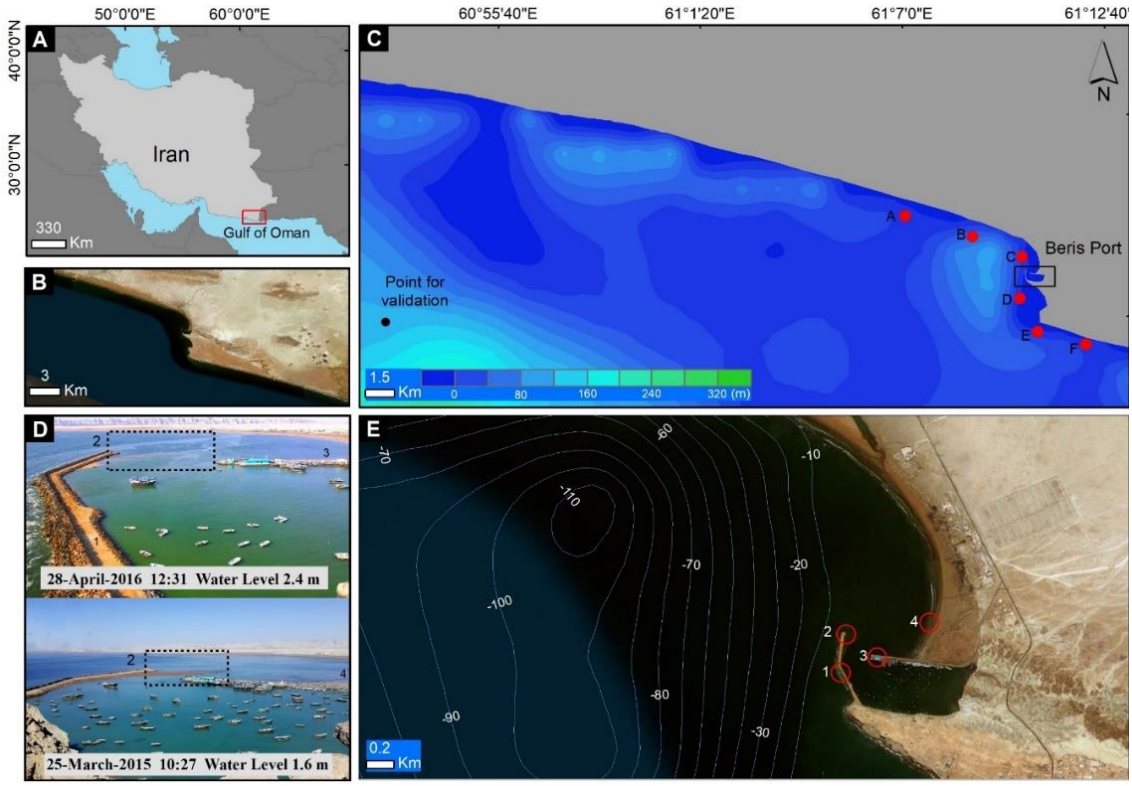

Figure 1. A) Location of Beris Port, B) Beris Port in eastern Chabahar and southern Iran. C) Bathymetry map of the study area (taken from SRTM15+ database corrected with local data), and the position of six points to extract model results. D) Beris Port image in two different tidal phases (28th of April 2016, with a water level of 2.4 m, and 25th of March 2015, with a water level of 1.6 m) (in the black box, the accretion in the low tide phase is evident). E) Beris Port satellite image: 1: the main arm of the breakwater, 2: entrance to the port, 3: the subsidiary breakwater arm and 4: the coastal part of the subsidiary arm

2.2. Numerical model

MIKE 21, created by the Danish Hydraulic Institute (DHI), is utilized for the analysis of wave and current patterns. This software package is suitable for simulating water level, currents, and waves in various types of water bodies, including river entrances, gulf interiors, coastal areas, and both shallow and deep waters [23, 24, 12]. MIKE 21 is based on the principles of shallow water equations and the depth-integrated incompressible Reynolds averaged Navier-Stokes equations. The Spectral Waves (SW) module simulates the growth, decay and transformation of wind-generated waves and swell for offshore and coastal areas. In this module, the waves are described using the density spectrum $N(\sigma.\theta)$, where σ represents the relative angular frequency $(\sigma = 2\pi f)$ and θ represents the direction of wave propagation. The equation governs the behavior of these waves is the wave action balance equation, which can be formulated in either cartesian or spherical coordinates (Eq. 1) [25].

$$\frac{\partial N}{\partial t} + \nabla,(\vec{v}N) = \frac{s}{\sigma} \quad \rightarrow \frac{\partial}{\partial t}N + \frac{\partial}{\partial x}C_x N + \frac{\partial}{\partial y}C_y N + \frac{\partial}{\partial \sigma}C_\sigma N + \frac{\partial}{\partial \theta}C_\theta N = \frac{s}{\sigma} \tag{1}$$

where, N represents the density of wave action, σ refers to the relative angular frequency, and θ represents the direction of the wave. C_x, C_y, C_σ, and C_θ are characteristics that describe the celerity of the wave in geographical and spectral coordinate systems. s is the term that represents the combination of five different energy sources which are described in Eq. 2.

$$s = s_{in} + s_{nl} + s_{ds} + s_{bot} + s_{surf} \tag{2}$$

s_{in}, represents the energy generated by the wind, s_{nl} represents the transfer of wave energy resulting from non-linear wave-wave interaction, s_{ds} represents the dissipation of wave energy caused by white capping, s_{bot} represents the dissipation due to bottom friction, and s_{surf} represents the dissipation of wave energy resulting from breaking induced by changes in water depth [26, 27].

In the Hydrodynamic (HD) module, Eq. 3 to 6 are governed for the conservation of mass and momentum. These equations are utilized to simulate the changes in water level and flow [28].

$$\frac{\partial \zeta}{\partial t} + \frac{\partial p}{\partial x} + \frac{\partial q}{\partial y} = \frac{\partial D}{\partial t} \tag{3}$$

$$\frac{\partial p}{\partial t} + \frac{\partial}{\partial x}\left(\frac{p^2}{h}\right) + \frac{\partial}{\partial y}\left(\frac{pq}{h}\right) + gh\frac{\partial \zeta}{\partial x} + \frac{gp\sqrt{p^2+q^2}}{c^2,h^2} - \frac{1}{\rho_w}\left[\frac{\partial}{\partial x}(h\tau_{xx}) + \frac{\partial}{\partial y}\left(h\tau_{xy}\right)\right] - \Omega_q - fvv_x + \frac{h}{\rho_w}\frac{\partial}{\partial_x}(\rho_a) = 0 \tag{4}$$

$$\frac{\partial q}{\partial t} + \frac{\partial}{\partial y}\left(\frac{q^2}{h}\right) + \frac{\partial}{\partial x}\left(\frac{pq}{h}\right) + gh\frac{\partial \zeta}{\partial x} + \frac{gp\sqrt{p^2+q^2}}{c^2,h^2} - \frac{1}{\rho_w}\left[\frac{\partial}{\partial y}\left(h\tau_{yy}\right) + \frac{\partial}{\partial x}\left(h\tau_{xy}\right)\right] - \Omega_p - fvv_y + \frac{h}{\rho_w}\frac{\partial}{\partial_{xy}}(\rho_a) = 0 \tag{5}$$

The mentioned equations establish a relationship between the water depth $(h(x.y.t))$, the temporal variation in water level $(d(x.y.t))$, and the actual water level $(\zeta(x.y.t))$ as described in Eq. 6.

$$h(x.y.t) = d(x.y.t) - \zeta(x.y.t) \tag{6}$$

where, $p.q\ (x\ .y\ .t)$ is flux of density in the x and y direction, g is gravitational acceleration, $f(v)$ is wind friction, $V(x)\ and\ V(y)$ are wind speed component in x and y direction, $p_a\ (x\ .y\ .t\ )$ is atmospheric pressure, ρ_w is water density, $\tau_{xx}.\tau_{xy}\ and.\tau_{yy}$ are shear stress components, t is time and $\Omega\ (x\ .y\ )$ is Coriolis effect [28].

2.2.1. Input data and model settings

The unstructured mesh used for modeling consists of 1214 nodes and 2215 elements. The domain covers latitudes between 24.7743˚ and 25.2810˚ N and longitudes between 60.6304˚ and 61.4637˚ E, an approximate range of 85.5 km long and 56.2 km wide. To create a bathymetry file, topography data developed by the USGS EROS institute "SRTM15+ Estimated Topography 15 arc seconds resolution" was used [29]. These data were modified using local depth data collected in Beris Port and navigation charts from Sonar Chart [30] (Fig. 1 C).

In order to apply wind data to the model, 6-hour ECMWF-ERA40 data for the year 2018 were used [31]. Wind data was prepared using ECMWF atmospheric model with resolution of 0.125˚ × 0.125˚ in the form of a NetCDF file. 10 meters u and v wind components were converted to speed (m/s) and direction (degree) and entered into the model as varying in time and domain. A wind rose (Fig. 2 B) clearly indicates that 55.4% of the winds were S-SW and the maximum wind intensity was 6 m/s. Water level data collected from National Cartographic Center of Iran in Chabahar station were applied to the western boundary of the model. The maximum water level recorded in 2018 was 2.8 m and the average was 1.66 m (Fig. 2 A).

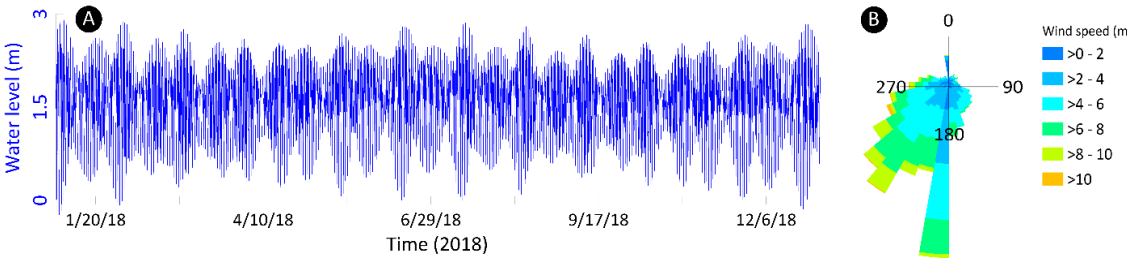

Figure 2. A) Water level time series for the year 2018 at Chabahar port (from National Cartographic Center of Iran). B) Wind rose of Beris Port region (from ECMWF-ERA40)

The Joint North Sea Wave Project (JONSWAP) spectrum with the fetch of 100 km was considered for wave simulation in the model [9]. Using the ECMWF ocean model, significant wave height (H_S), Tp (Spectral peak period) and MWD (Mean wave direction) data were applied to the open boundaries in the form of varying in time and constant along the line.

The eddy viscosity and bed resistance parameter of the Hydrodynamic (HD) module and wave breaking, bottom friction, and white capping of the Spectral Waves (SW) module was used for sensitivity analysis and calibration [12]. ECMWF ocean model results and satellite altimetry data were used to calibrate the model [32, 31], and to derive the best calibrated coefficients (Table 1).

Table 1. Parameters used for simulating hydrodynamics in the study region

#	Equations or parameters	Applied in this investigation	Module
1	Bathymetry	SRTM15+	Domain
2	Energy transfer	Quadruplet-wave interaction	SW/HD
3	Basic Equations	fully spectral formulation	SW
4	White capping	cdis=4.5 and Delta=0.5	SW
5	Wave breaking	Gamma data 0.8 and Alpha=1	SW
6	Bottom friction	Nikuradse roughness =0.04	SW
7	Current Conditions	HD simulation	SW
8	Wind forcing	Data from ECMWF institute	SW
9	Water level	Water level of Chabahar Port	HD
10	Eddy viscosity	Smagorinsky formulation= 0.28	HD
11	Wave Radiation	SW simulation	HD
12	Bed Resistance	Chezy number= 32	HD
13	Density	Barotropic	HD
14	Flood and Dry	Standard flood and dry	HD
15	Coriolis Forcing	Varying in domain	HD

2 Model validation results

To verify the accuracy of the model results, data from ECMWF and satellite altimetry in 2018 were utilized. The H_S from the ECMWF ocean model was compared to the SW module output (Fig. 3), while the u and v velocity components from the HD module output were compared to available satellite altimetry data from NOAA CoastWatch/OceanWatch (Fig. 4). The station used for data comparison is indicated as the "Point of validation" in Fig. (1 C). To assess the model's performance, statistical parameters such as root mean square error (RMSE), correlation coefficient (CC), bias parameter (BIAS), and index of dispersion (SI) were employed (Table 2). Based on the CC index, the correlation coefficients for H_S, v, and u are 0.987, 0.658, and 0.649, respectively.

Table 2. Statistical parameters for evaluating simulated Hs compared to the ECMWF ocean model data and simulated current components (u, v) with those of CoastWatch/OceanWatch satellite altimetry

			RMSE	CC	BIAS	S1
Parameters	Formula		$\sqrt{\frac{\sum_{i=1}^{N}(S_i - M_i)^2}{N}}$	$\frac{\sum_{i=1}^{N}(S_i - \bar{S})\,(M_i - \bar{M})}{\sqrt{\sum_{i=1}^{N}(S_i - \bar{S})^2 \sum_{i=1}^{N}(M_i - \bar{M})^2}}$	$\sum_{i=1}^{N}\frac{1}{N}(S_i - M_i)$	$\frac{\text{RMSE}}{\sqrt{\frac{1}{N}\sum_{i=1}^{N} M_i}}, 100$
	Reference		[34, 9]	[35]	[36]	[36, 37]
Module	SW	H_S	0.099	0.982	-0.026	11.171
	HD	u	0.082	0.66	-0.045	66.706
		v	0.079	0.65	0.012	30.490

N is the number of observations, S represents the simulated values, and M represents the base values

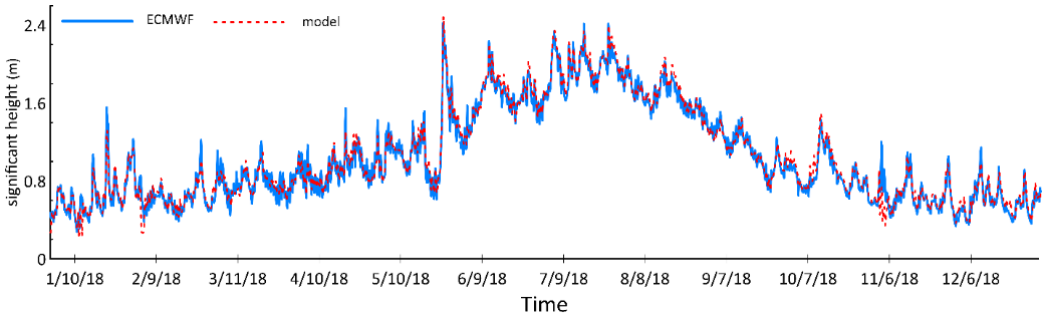

Figure 3. Simulated Hs time series derived out from the model (red) and from ECMWF ocean model (blue)

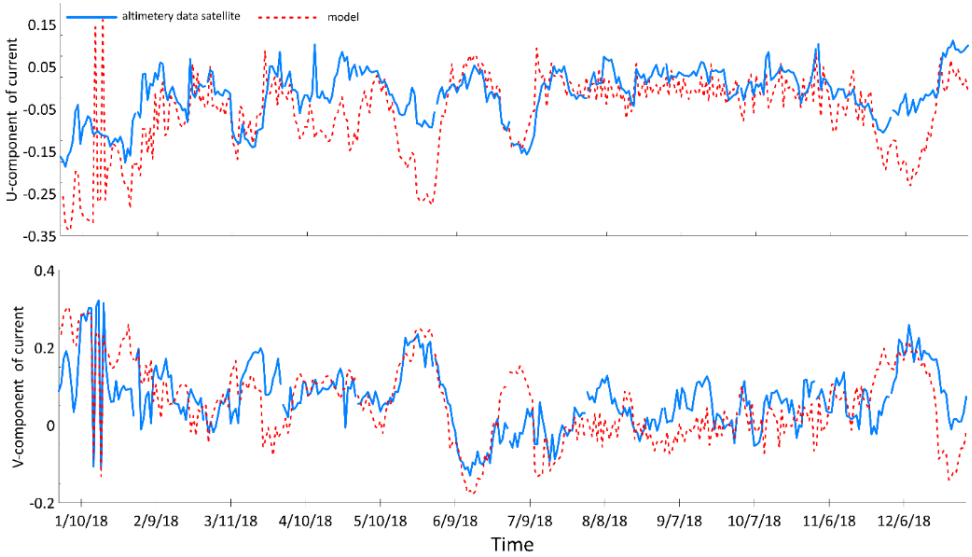

Figure 4. Simulated u and v component of current velocity derived from the model (red) and from CoastWatch/OceanWatch satellite altimetry (blue)

2.3. Remote Sensing images

RS images obtained from Landsat 5 and 8 [38, 39, 40] were used to investigate the historical shoreline changes around Beris Port. Radiometric and atmospheric corrections were applied to the images using ENVI 5.3 software. All images were georeferenced to UTM/WGS84 projection. Radiometric and atmospheric correction includes subtraction of the atmospheric contribution, reduction of illumination, viewing angles, terrain effects, and sensor calibration [41]. For all these corrections again ENVI 5.3 software was employed [42, 43].

To verify the shoreline, land and water features should be identified and be separated. The NDWI index was used for this purpose (Eq. 1) [44].

$$NDWI = \frac{B_{GREEN} - B_{NIR}}{B_{GREEN} + B_{NIR}} \quad (1)$$

where, B_{Green} is the green band (Landsat-5 TM band 2, and Landsat-8 OLI band 3), and B_{NIR} is the near infrared band (Landsat-5 TM band 4, Landsat-8 OLI band 5). The central wavelength of band 2 in sensor TM and OLI is 0.560 µm, the central wavelength of band 4 in sensor TM is 0.830 µm, and the central wavelength of band 5 on the OLI sensor is 0.865 µm.

After applying the NDWI index, we used unsupervised classification K-Means, with an iteration number of 30 and 2 clusters, to divide the images into two categories of land and water features (eq. 2) [45, 46].

$$e^2(K) = \sum_{k=1}^{K} \sum_{i \in C_k} (x_i - c_k)^2 \quad (2)$$

where,c_k is the centroid of the cluster C_k, and K is the number of clusters (known a priori) [45].

3. Results

3.1. Significant wave height pattern in the area

Analyzing averaged seasonal wave pattern (extracted from SW model), we found that H_S is much higher in summer than that during the other seasons (Fig. 5); reaching up to 2.0 m offshore and up to 1.4 m nearshore. From July until the end of September persistent and intense southwesterly winds are dominant over the Arabian Sea and eastern parts of the Gulf of Oman [21], which might be the reason for increasing wave height during summer. With the onset of autumn, wave height decreases, with offshore wave heights of up to 0.8 m and nearshore wave heights of less than 0.6 m. In winter the wave height reaches its minimum values; offshore wave height is between 0.6 and 0.4 m, and nearshore wave height is less than 0.4 m. With the onset of spring the wave height somehow increases, so the offshore wave height exceeds 0.8 m (Fig. 5). The average annual pattern of waves shows that the direction of the waves in the area is mainly from the south-southwest. In the area near Beris port, due to the curvature of the shoreline, the direction of the waves is from the southeast. The main basin of Beris Port always hosts calm waves. The wave height in the western section of Beris Port is impacted by the breakwater, resulting in significantly reduced waves compared to the surrounding area (Fig. 5). A sudden decrease in wave height in this area could contribute to sedimentation (See Fig. 1 D).

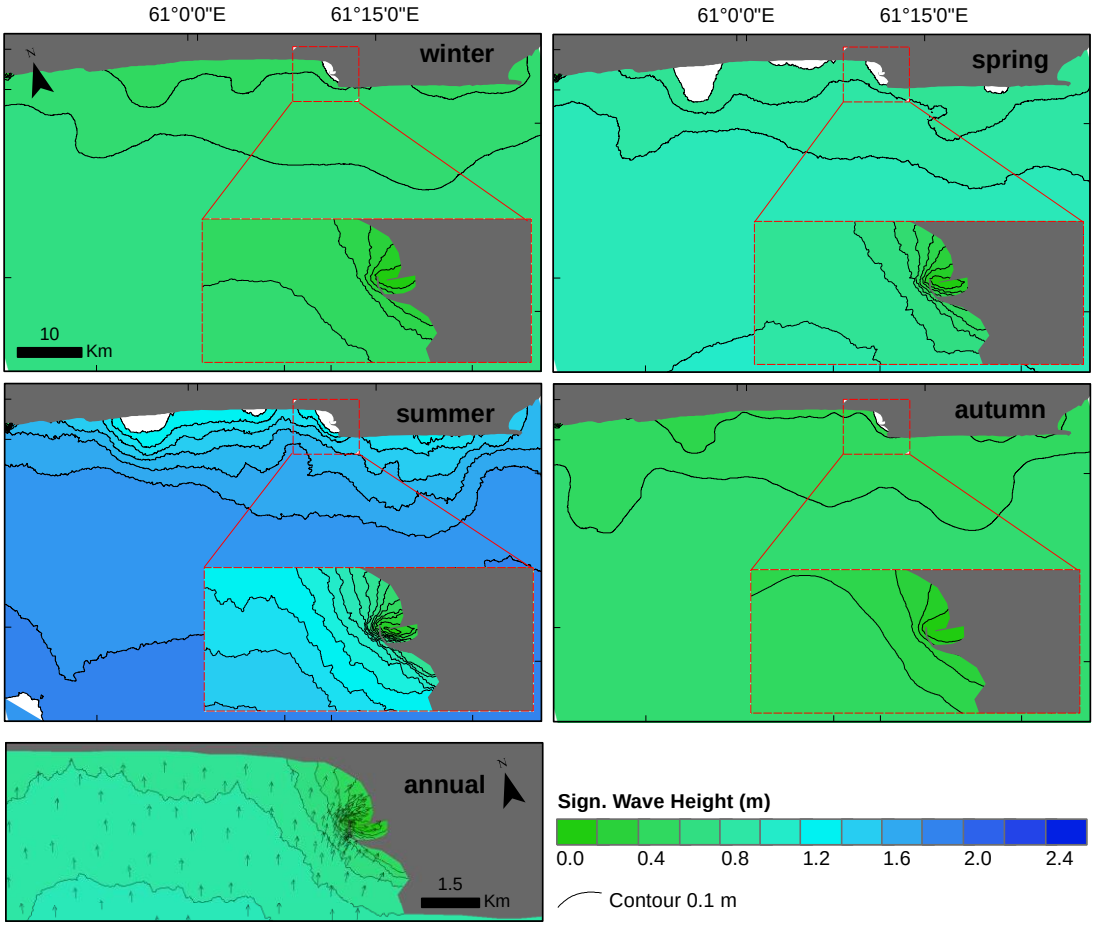

Figure 5. Map of averaged seasonal and annual significant wave height (Hs) around Beris Port, obtained from the SW model

3.2. Current pattern in the area

The seasonal current speed contours (extracted from HD model) show that during winter the currents are stronger than that during other seasons (Fig. 6). In winter the maximum current speed is about 0.5 m/s (offshore). Current speed along the shoreline varies significantly (less than 0.1 m/s). With the onset of spring, the maximum current speed is 0.275 m/s offshore, and 0.025 m/s nearshore. During the summer current speed decreases in a way that offshore current speed is less than 0.125 m/s, although nearshore current speed is still more or less the same (less than 0.025 m/s).

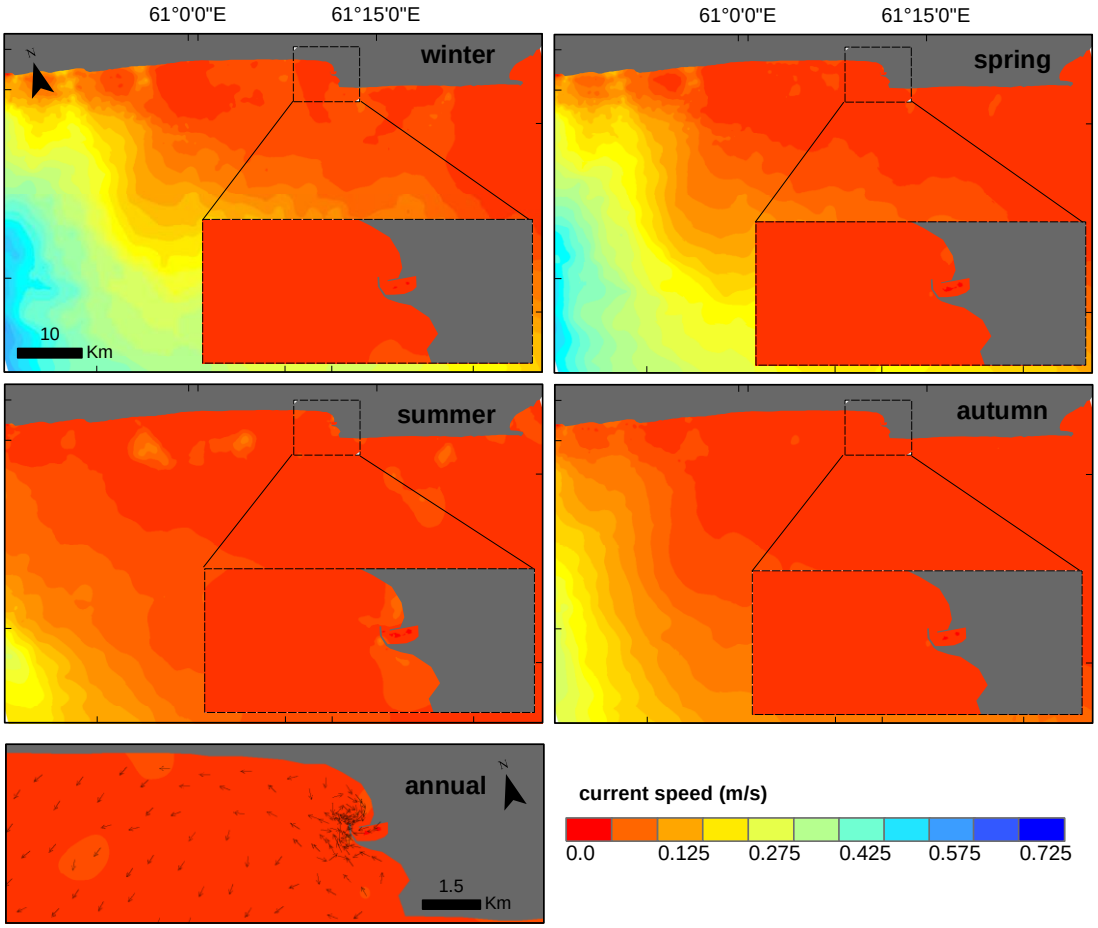

Figure 6. Map of averaged seasonal and annual current speed contours of Beris Port area, obtained from the HD model

During the year, the offshore current direction (Fig. 7) is generally west-northwest and northwest (especially in winter and spring), but near the shore the current direction is not uniform (Fig. 7). In both Fig. 6 and 7 formations of small eddies are evident, especially during three seasons of winter, spring and summer. The formation of these eddies along the coastline is the reason for the erosion and sedimentation processes in this region [47, 48]. Averaged annual current plots also show that the current direction in the northern part of Beris Port (labeled 4 in Fig. 1 E) is against the general pattern of the region, and the current direction in this part is south-southeast and south during the entire year, which may form eddies and cause the tendency for accretion in this area.

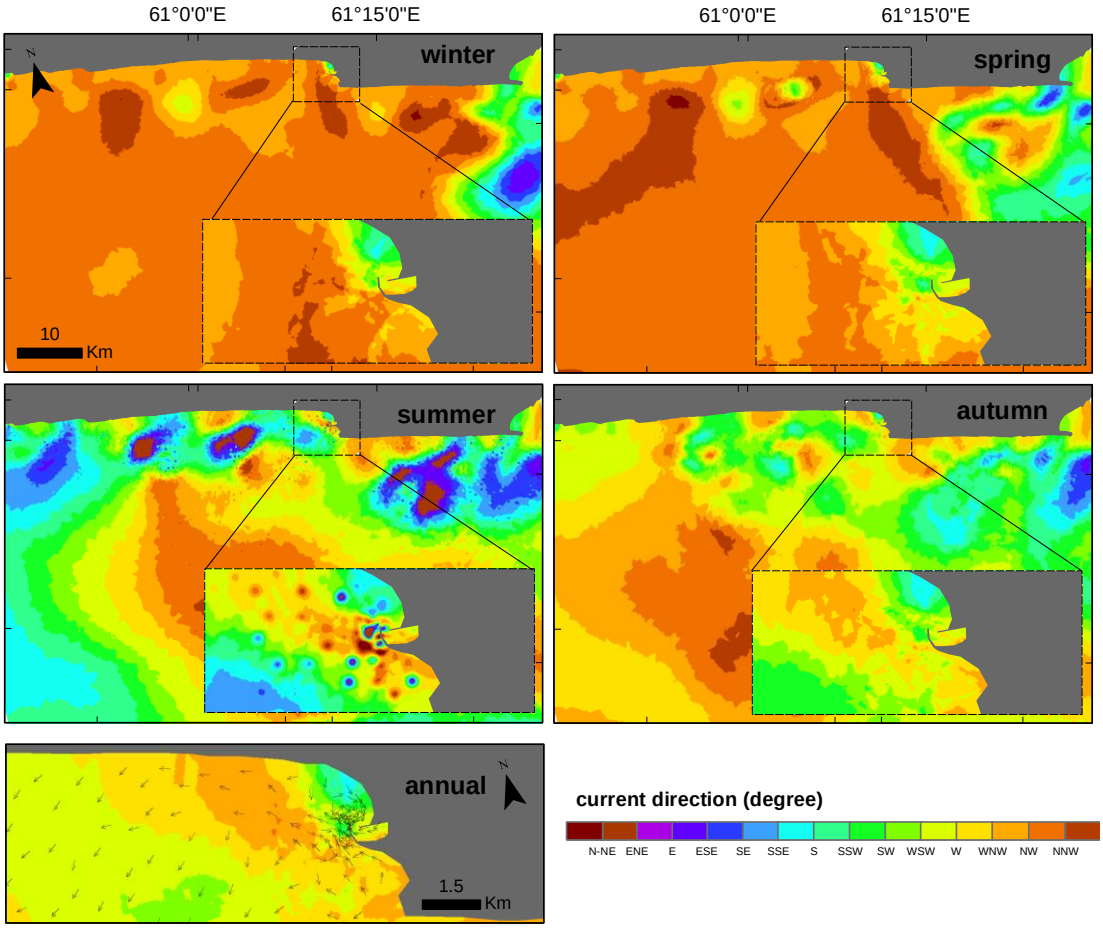

Figure 7. Map of averaged seasonal and annual current direction in the Beris Port area, obtained from the HD model

3.3. Satellite images of the area

In order to validate the results derived from the model, satellite images for three different dates were employed (Fig. 8); before the construction of the breakwater (1988), right after the construction of the breakwater (1990) and for the year 2019. All images were obtained during low-tide conditions (Fig. 8 A). In Fig. 8 C shorelines of the year 1988 (red), 1990 (green), and 2019 (blue) are outlined. According to this plot the shoreline of the northern part of the Beris Port has accreted significantly (accretion of about 20.97 ha), (Fig. 8 C, light green), while in the upper part erosion is evident (~14.84 ha), (Fig. 8 C, light red).

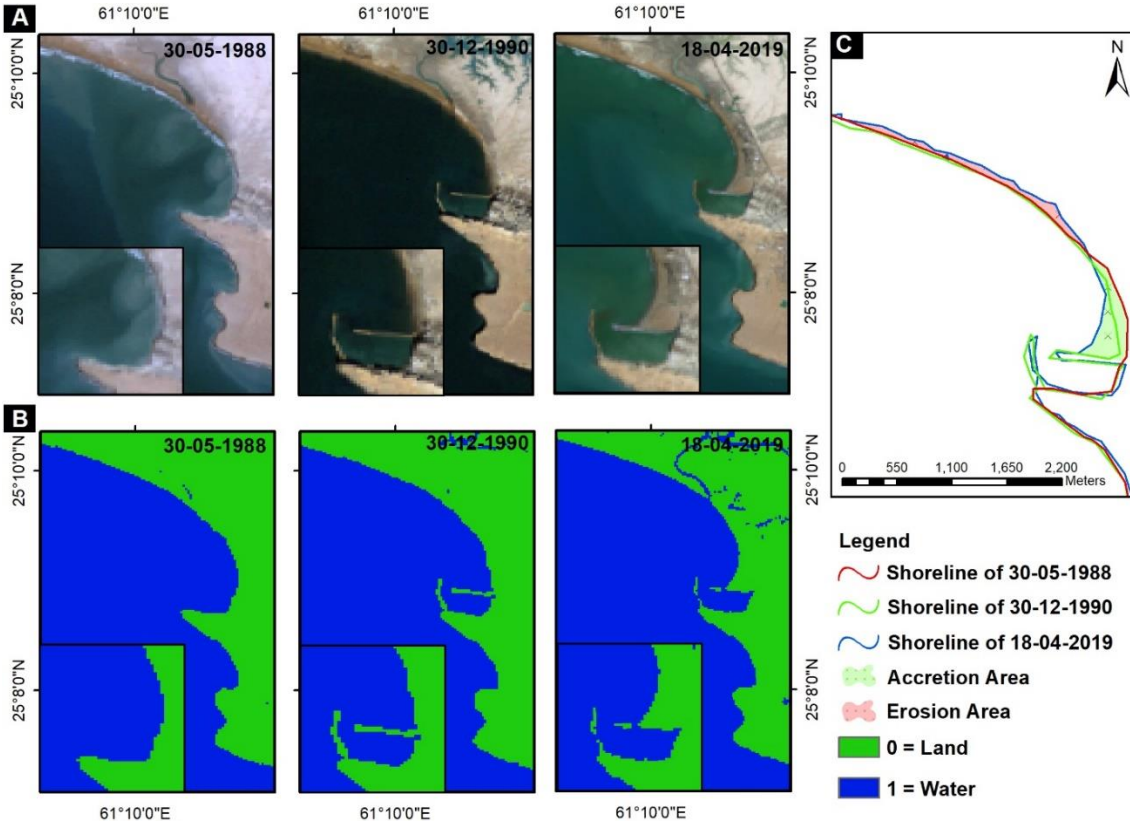

Figure 8. A) Satellite image at three different dates of 1988, 1990 and 2019. B) Images after applying the NDWI index and unsupervised K-means classification technique. C) The conversion of raster to polygon and line

4. Discussion

Based on the analysis of wave patterns (Fig. 5) and current movements (Fig. 6) around Beris Port, it has been observed that sedimentation occurs predominantly, particularly in the vicinity of the breakwater. Sayehbani and Ghaderi [6], in their study on sedimentation mechanisms around Beris Port over a one-month period, also suggested that the weak clockwise current on the western side of the port may play a significant role in the sedimentation process near the breakwater arms. Additionally, RS images provide further evidence of shoreline accretion near the port (Fig. 8 C).

In order to study the precise effect of the hydrodynamic conditions on the Beris Port, we focused on the data obtained from 6 stations (A to F in Fig. 1 C) during the year 2018. The distance of the selected stations from the shoreline is approximately 400 to 600 m, and the distance between the stations is approximately between 2 and 3.2 km. These stations are selected based on observations of wave and current patterns in Figs. 5-7. Summarized information about the stations is available in Table 3.

Table 3. Information on 6 selected stations in the vicinity of Beris Port (see Fig. 1 C)

St.	Coordinates		SW*		HD**		Location in the area
	latitude	longitude	Hs (m)	Direction	Current speed (m/s)	Direction	
A	25.17476	61.11791	0.82 ± 0.4	S	0.035 ± 0.031	SW	near the shore, away from the port (west)
B	25.16509	61.14941	0.80 ± 0.3	S	0.008 ± 0.005	W	western part of port
C	25.1558	61.1727	0.57 ± 0.2	SW	0.017 ± 0.006	S	northern part of port
D	25.13623	61.1717	0.75 ± 0.3	SSW	0.027 ± 0.013	WNW	southern part of port
E	25.12058	61.17978	0.82 ± 0.3	SSW	0.027 ± 0.020	SW	top of the coastline curvature
F	25.11460	61.20238	0.84 ± 0.4	S	0.036 ± 0.034	WSW	near the shoreline away from the port (east)

* Average annual wave height and direction of SW model
** Average annual current speed and direction of HD model

The wave direction histograms (green histogram in Fig. 9) of all the stations show the domination of southern waves (S to SW). It should be emphasized that for two of the stations (C and D), the direction tends to be mainly southwestward (SW); probably due to the curvature of the coast. The seasonal wave dot plot (Fig. 9) shows that the wave height is higher in summer (red dots) at all stations (reaching heights of up to 1.5 m). The decrease in wave height at station C (less than 1 m) is due to the Beris Port breakwater structure. During summer and autumn when the wind is mainly from the south (S) H_S is normal to the shore and is relatively large, while during spring and winter when the wind is mainly from southwest (SW) to southeast (SE) H_S is inclined relative to the shore and is smaller (below 1 m). A longshore current, which might cause an increase in sediment transport along the coast would be expected during spring and winter (Fig. 8 C, red polygon).

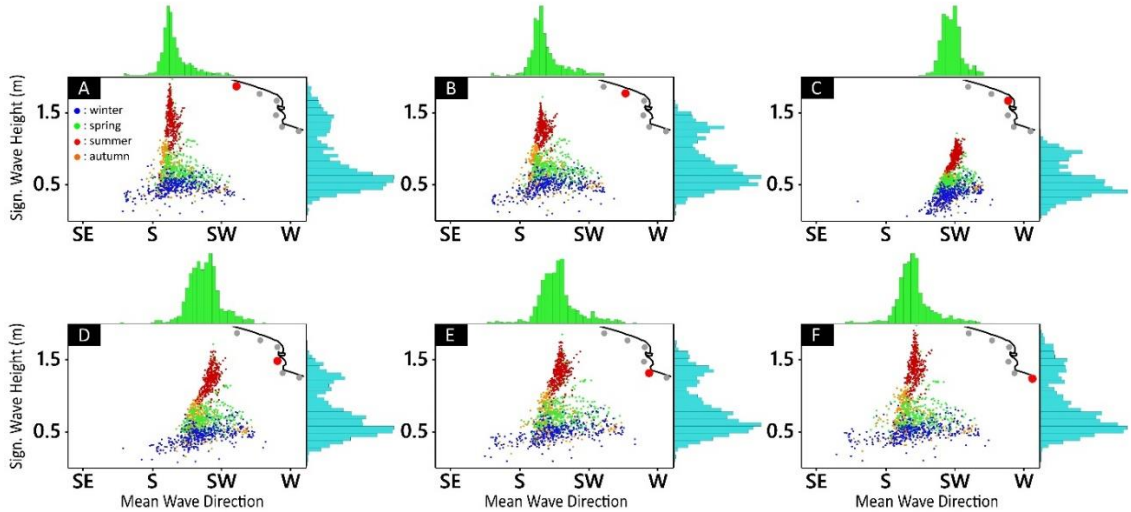

Figure 9. Wave direction histogram (green), Hs histogram (cyan), and dot plot of seasonal wave pattern at 6 stations (A-F)

The current direction (green histograms in Fig. 10) at stations A and F (far from the Beris Port structure) is relatively similar through the year, with two peaks of occurrence, one to the W and another to the ESE. Both of these stations present the maximum current speeds (dot plots, Fig. 10). The direction at stations B is mainly WNW, the direction in station C and D is mostly to the N and S, but at D the direction of N is more frequent (Fig. 10). It should be noted that the current speeds at stations B and C, influenced by the breakwater structure, is relatively low compared with that of station D. Current speed (cyan histograms of Fig. 10) at stations B, C, and D are relatively low during the entire year compared with that of the three other stations.

Model results show the formation of small clockwise eddies around the port (Fig. 6 and 7), which is likely to be due to the geomorphology of the area and the breakwater structure. These eddies can influence the accretion and erosion in the area, which is also claimed in other studies [48, 47]. Imagery results also confirm accretion adjacent to the port (green polygon in Fig. 8) and erosion (red polygon in Fig. 8) in the upper part of the port. This trend of shoreline transformation has also been reported previously [18]. Overall, the currents in the western part of the port are relatively calm (Fig. 10 B and C), which can cause accretion. Since the construction of the breakwater till the year 2019 accretion is observed around the west side of the port and port entrance, (Fig. 1 D and 8 C). This is in contrast with the previous studies [17, 18], which has been claimed that the entrance of the port is safe from accretion.

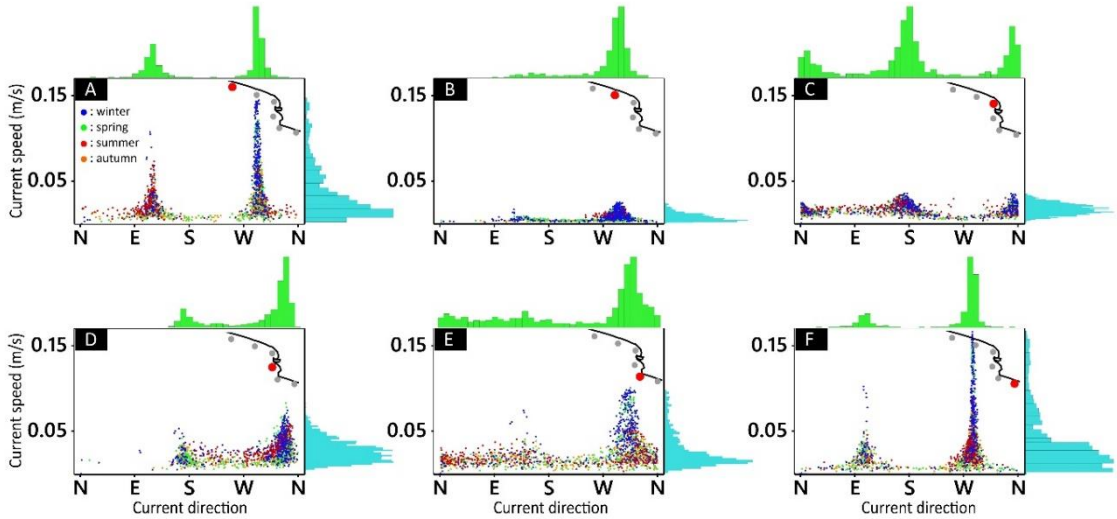

Figure 10. Current direction histogram (green), current speed histogram (cyan), and dot plot of seasonal current pattern at six stations (A-F)

Our model results revealed that the breakwater is responsible for the accumulation of sediment inside the port, which is aligned with the results reported previously [6]. In that research focusing on a short period of time, the researcher claimed that the wave height at eastern part of the port (referred to as point D in this study), did not influence by the presence of the breakwater, but the current pattern was influenced significantly. According to their results the western part of the port (referred to as point C in this study), the wave height experienced a significant reduction due to the presence of the breakwater. The wave height was reported to be within the range of 0.7 to 0.8 m, which aligns well with the summer season data in this study (represented by the red points in figure 9-C). They also reported the decrease of current in the western part influenced by presence

of the breakwater, which is again aligns well with the results observed in this study (see figure 10-C). Overall, the construction of the breakwater is influenced the current pattern in both side of the breakwater, and wave pattern of the western part. This variation in wave and current pattern of the area is responsible for the shoreline change.

5. Conclusions

In this study, we have utilized both hydrodynamic simulation and RS imagery to investigate and illustrate the factors that influence the transformation of the shoreline around Beris fishery port in the Makran region, located on the northern coast of the Gulf of Oman. It has been reported that the area is experiencing significant accretion near the breakwater arms. To achieve this, we have used the SW and HD modules of MIKE 21 to simulate the wave and current patterns in the area for an entire year. Additionally, we have employed satellite images from Landsat 5 and 8 on three different dates (prior to breakwater construction, immediately after construction, and for the year 2019) to detect changes in the shoreline using GIS technique.

Annual averaged wave height near the port is about 0.57 m, and in summer when strong winds blow, the wave height is less than 1.0 m. Away from the port the wave height in summer reaches up to 1.5 m. Annual averaged current speed is about 0.01 m/s, which is the desirable condition for the safe navigation of large and small fishing boats. However, the inclination of the incident wave to the shore causes the formation of a longshore current, which causes transportation of transferred sediment and accretion and deposition along the shore. Calm conditions of current and wave around the port, simultaneous with clockwise eddy formation around the port, which is opposite to the dominant current are responsible for accretion inside the port and erosion outside the port. According to our results variation of current pattern forced to the area due to the presence of the breakwater is the main reason for the huge shoreline change in the area. Our findings contradict previous studies but align with field observations regarding shoreline changes. Therefore, we believe that the simultaneous use of hydrodynamical data and satellite imagery is a reliable technique for comprehending and managing the geomorphological behavior around anthropogenic structures.

References

1. Parthasarathy, K.S.S., Deka, P.C., (2019). Remote sensing and GIS application in assessment of coastal vulnerability and shoreline changes: a review. ISH J. Hydraul. Eng. 00, 1–13. https://doi.org/10.1080/09715010.2019.1603086.
2. Van, T.T., Binh, T.T., (2008). Shoreline change detection to serve sustainable management of coastal zone in Cuu Long Estuary, in: International Symposium on Geoinformatics for Spatial Infrastructure Development in Earth and Allied Sciences.
3. Bird, E.C.F., Ongkosongo, O.S.R., (1981). Environmental changes on the coasts of Indonesia (resource management).
4. Leont'yev, I.O., Akivis, T.M., (2020). The Effect of a Groin Field on a Sandy Beach. Oceanology 60, 412–420. https://doi.org/10.1134/S0001437020030042
5. Oost, A.P., Hoekstra, P., Wiersma, A., Flemming, B., Lammerts, E.J., Pejrup, M., Hofstede, J., der Valk, B., Kiden, P., Bartholdy, J., others, (2012). Barrier island management: Lessons from the past and directions for the future. Ocean Coast Manag 68, 18–38.
6. Sayehbani, M., Ghaderi, D., (2019). Numerical Modeling of Wave and Current Patterns of Beris Port in East of Chabahar-Iran. Int. J. Coastal Offshore Eng. 3, 21–29.

7. Dereli, M.A., Tercan, E., (2020). Assessment of Shoreline Changes using Historical Satellite Images and Geospatial Analysis along the Lake Salda in Turkey. Earth Sci. Inf. 13, 709–718. https://doi.org/10.1007/s12145-020-00460-x
8. Ghaderi, D., Rahbani, M., (2020a). Shoreline change analysis along the coast of Bandar Abbas city, Iran using remote sensing images. Int. J. Coastal Offshore Eng. 4, 51–64. https://doi.org/10.22034/ijcoe.2020.149346
9. Anton, I.A., Rusu, L., Anton, C., (2019). Nearshore wave dynamics at Mangalia beach simulated by spectral models. J. Mar. Sci. Eng. 7, 206.
10. Pradhan, U.K., Mishra, P., Mohanty, P.K., Panda, U.S., Ramanamurthy, M. V, (2020). Modeling of tidal circulation and sediment transport near tropical estuary, east coast of India. Reg. Stud. Mar. Sci. 101351.
11. Mahmoodi, A., Lashteh Neshaei, M.A., Mansouri, A., Shafai Bejestan, M., (2020). Study of Current-and Wave-Induced Sediment Transport in the Nowshahr Port Entrance Channel by Using Numerical Modeling and Field Measurements. J. Mar. Sci. Eng. 8, 284.
12. Pakhirehzan, M., Rahbani, M., Malakooti, H., (2018). Numerical Study of Winter Shamal Wind Forcing on the Surface Current and Wave Field in Bushehr's Offshore Using MIKE21. Int. J. Coastal Offshore Eng. 2, 57–65.
13. Mahamud, U., Takewaka, S., (2018). Shoreline Change around a River Delta on the Cox's Bazar Coast of Bangladesh. J. Mar. Sci. Eng. 6, 80. https://doi.org/10.3390/jmse6030080
14. Zhang, K., Li, Q., Zhang, J., Shi, H., Yu, J., Guo, X., Du, Y., (2022). Simulation and Analysis of Back Siltation in a Navigation Channel Using MIKE 21. J. Ocean Univ. China 21, 893–902. https://doi.org/10.1007/s11802-022-5052-9
15. Abualtayef, M., Rabou, M.A., Afifi, S., Rabou, A.F.A., Seif, A.K., Masria, A., (2021). Change detection of Gaza coastal zone using GIS and remote sensing techniques. J.Coastal Conserv. 25, 36.
16. Nassar, K., Mahmod, W.E., Fath, H., Masria, A., Nadaoka, K., Negm, A., (2019). Shoreline change detection using DSAS technique: Case of North Sinai coast, Egypt. Mar. Georesour. Geotechnol. 37, 81–95. https://doi.org/10.1080/1064119X.2018.1448912
17. Hajivalie, F., Soltanpour, M., (2007). Beris fishing port, interfering in the equilibrium shape of a bay, in: Coastal Eng. World Scientific, pp. 3843–3850.
18. Ardani, S., Soltanpour, M., (2015). Modelling of sediment transport in Beris fishery port. Civ. Eng. Infrastruct. J. 48, 69–82. https://doi.org/10.1007/s11852-021-00825-4
19. Ghaderi, D., Rahbani, M., (2020b). Detecting shoreline change employing remote sensing images (Case study: Beris Port-east of Chabahar, Iran). Int. J. Coastal Offshore Eng. 3, 1–8. https://doi.org/10.29252/ijcoe.3.4.1
20. Motamedi, H., Rahbani, M., Harifi, A., Ghaderi, D., (2020). The choice between Radial Basis function and Feed Forward Neural Network to predict long term tidal condition. Int. J. Coastal Offshore Eng. 4, 1–9. https://doi.org/10.29252/ijcoe.4.1.1
21. Chaichitehrani, N., Allahdadi, M.N., (2018). Overview of wind climatology for the Gulf of Oman and the northern Arabian Sea. Am. J. Fluid Dyn. 8, 1–9.
22. Pous, S.P., Carton, X., Lazure, P., (2004). Hydrology and circulation in the Strait of Hormuz and the Gulf of Oman—Results from the GOGP99 Experiment: 2. Gulf of Oman. J. Geophys. Res.: Oceans 109.
23. Divinsky, B. V, Kuklev, S.B., Zatsepin, A.G., (2017). Numerical simulation of an intensive upwelling event in the northeastern part of the Black Sea at the IO RAS hydrophysical testing site. Oceanology 57, 615–620.

24. Moghaddam, E.I., Allahdadi, M.N., Hamedi, A., Nasrollahi, A., (2018). Wave-induced currents in the northern Gulf of Oman: a numerical study for Ramin Port along the Iranian coast. Am. J. Fluid Dyn. 8, 30–39.
25. Komen, G. J., Cavaleri, L., Donelan, M., Hasselmann, K., Hasselmann, S., & Janssen, P. A. E. M., (1996). Dynamics and modelling of ocean waves (p. 554).
26. Remya, P.G., Kumar, R., Basu, S., (2014). An assessment of wind forcing impact on a spectral wave model for the Indian Ocean. Journal of Earth System Science 123, 1075–1087. https://doi.org/10.1007/s12040-014-0450-z
27. DHI, M., (2017). MIKE 21 Spectral Wave Module, Scientific Documentation. Hørsholm, Denmark: DHI Water Environment Health.
28. DHI Group, (2017). MIKE 21 Flow Model: Hydrodynamic Module User Guide. DHI Water & Environment: Brisbane, Australia.
29. Becker, J.J., Sandwell, D.T., Smith, W.H.F., Braud, J., Binder, B., Depner, J.L., Fabre, D., Factor, J., Ingalls, S., Kim, S.H., others, (2009). Global bathymetry and elevation data at 30 arc seconds resolution: SRTM30_PLUS. Mar. Geod. 32, 355–371.
30. Herrera, J., Hernández-Hamón, H., Fajardo, L., Ardila, N., Franco, A., Ibeas, A., (2022). Colombian Caribbean Bathymetry for an OTEC System Location. Journal of Marine Science and Engineering 10, 519. https://doi.org/10.3390/jmse10040519
31. Berrisford, P., Dee, D., Fielding, K., Fuentes, M., Kallberg, P., Kobayashi, S., Uppala, S., (2009). The ERA-interim archive. ERA report series 1–16.
32. Leuliette, E.W., Scharroo, R., (2010). Integrating Jason-2 into a multiple-altimeter climate data record. Mar. Geod. 33, 504–517.
33. NOAA CoastWatch/OceanWatch, (2019). Sea level Anomaly and Geostrophic Currents, multi-mission, global,optimal interpolation, gridded | NOAA CoastWatch & OceanWatch. URL https://coastwatch.noaa.gov/cw/satellite-data-products/sea-surface-height/sea-level-anomaly-and-geostrophic-currents-multi-mission-global-optimal-interpolation-gridded.html (accessed 8.18.20).
34. Cox, A.T., Swail, V.R., (2001). A global wave hindcast over the period 1958--1997: Validation and climate assessment. J. Geophys. Res.: Oceans 106, 2313–2329.
35. Kalra, R., Deo, M.C., (2007). Derivation of coastal wind and wave parameters from offshore measurements of TOPEX satellite using ANN. Coastal Eng. 54, 187–196.
36. Mahjoobi, J., Etemad-Shahidi, A., Kazeminezhad, M.H., (2008). Hindcasting of wave parameters using different soft computing methods. Appl. Ocean Res. 30, 28–36.
37. Rusu, E., (2018). An analysis of the storm dynamics in the Black Sea. Rom. J. Tech. Sci.-Appl. Mech 63, 131–146.
38. Bacino, G.L., Dragani, W.C., Codignotto, J.O., Pescio, A.E., Farenga, M.O., (2020). Shoreline change rates along Samborombón Bay, Río de la Plata estuary, Argentina. Estuarine Coastal Shelf Sci. 237, 106659. https://doi.org/10.1016/j.ecss.2020.106659
39. Abdul-Kareem, R., Asare, N.K., Angnuureng, D.B., Brempong, E.K., (2022). Shoreline Variability of a Bay Beach: The Case of Apam Beach, Ghana. Estuaries Coasts. https://doi.org/10.1007/s12237-022-01110-9
40. United States Geological Survey, (2020). EarthExplorer [WWW Document]. URL https://earthexplorer.usgs.gov/ (accessed 8.2.20).
41. Lillesand, T., Kiefer, R.W., Chipman, J., (2015). Remote sensing and image interpretation. John Wiley & Sons.

42. Do, A.T.K., Vries, S. de, Stive, M.J.F., (2019). The Estimation and Evaluation of Shoreline Locations, Shoreline-Change Rates, and Coastal Volume Changes Derived from Landsat Images. J. Coastal Res. 35, 56. https://doi.org/10.2112/JCOASTRES-D-18-00021.1
43. Masria, A., Nadaoka, K., Negm, A., Iskander, M., (2015). Detection of Shoreline and Land Cover Changes around Rosetta Promontory, Egypt, Based on Remote Sensing Analysis. Land 4, 216–230. https://doi.org/10.3390/land4010216
44. McFEETERS, S.K., (1996). The use of the Normalized Difference Water Index (NDWI) in the delineation of open water features. Int. J. Remote Sens. 17, 1425–1432. https://doi.org/10.1080/01431169608948714
45. Oliver, A., Muñoz, X., Batlle, J., Pacheco, L., Freixenet, J., (2006). Improving clustering algorithms for image segmentation using contour and region information. 2006 IEEE International Conference on Automation, Quality and Testing, Robotics, AQTR. https://doi.org/10.1109/AQTR.2006.254652
46. Rashmi, C., Chaluvaiah, S., Kumar, G.H., (2016). An Efficient Parallel Block Processing Approach for K -Means Algorithm for High Resolution Orthoimagery Satellite Images. Procedia Comput. Sci. https://doi.org/10.1016/j.procs.2016.06.025
47. Klonaris, G.T., Metallinos, A.S., Memos, C.D., Galani, K.A., (2020). Experimental and numerical investigation of bed morphology in the lee of porous submerged breakwaters. Coastal Eng. 155, 103591. https://doi.org/10.1016/j.coastaleng.2019.103591
48. Ouillon, S., (2018). Why and How Do We Study Sediment Transport? Focus on Coastal Zones and Ongoing Methods. Water 10, 390. https://doi.org/10.3390/w10040390